

Article

Conducting Research to Identify Key Features and Critical Nodes in the Coalescence and Instability of Pre-Fabricated Jointed Rock

Buchu Zhang ^{1,2} , Shichuan Zhang ^{1,2,*}, Baotang Shen ^{1,2}, Yangyang Li ^{1,2}, Shilong Song ¹ and Xuexian Han ¹

¹ College of Energy and Mining Engineering, Shandong University of Science and Technology, Qingdao 266590, China; 15621166605@163.com (B.Z.); 18253151805@163.com (B.S.); lyy1987718@126.com (Y.L.); 15265119571@163.com (S.S.); 18265523191@163.com (X.H.)

² Laboratory of Mine Disaster Prevention and Control, Shandong University of Science and Technology, Qingdao 266590, China

* Correspondence: zsc373260186@sdust.edu.cn

Abstract: The instability of jointed rock masses has been a persistent concern in China's underground geotechnical engineering, particularly regarding rock mass instability triggered by structural activation, such as faulting. This form of instability constitutes a significant type of dynamic geological hazard in the field of geotechnical engineering. Research on the mechanism of jointed rock mass instability typically concentrates on various characteristics associated with structural activation but frequently neglects the interplay between coalescence instability within the jointed zones and the intact zones, as well as the development and evolution of abrupt water channels. To delve into the coalescence instability characteristics between jointed and intact zones, this study conducted uniaxial compression tests on macro-scale pre-fabricated jointed sandstone. The research results show that the failure process of the specimen consists of a strong deviation linear stage, a sub-critical stage, and an unstable stage. The main failure process occurs during the sub-critical stage.

Keywords: jointed rock masses; coalescent failure; energy evolution; identification information



Citation: Zhang, B.; Zhang, S.; Shen, B.; Li, Y.; Song, S.; Han, X. Conducting Research to Identify Key Features and Critical Nodes in the Coalescence and Instability of Pre-Fabricated Jointed Rock. *Appl. Sci.* **2024**, *14*, 7905. <https://doi.org/10.3390/app14177905>

Academic Editor: Ricardo Castedo

Received: 30 July 2024

Revised: 22 August 2024

Accepted: 3 September 2024

Published: 5 September 2024



Copyright: © 2024 by the authors. Licensee MDPI, Basel, Switzerland. This article is an open access article distributed under the terms and conditions of the Creative Commons Attribution (CC BY) license (<https://creativecommons.org/licenses/by/4.0/>).

1. Introduction

In the surrounding rock of underground engineering projects, there are typically numerous geological discontinuities, such as fractures and faults, characterized by geological joints. These discontinuous and weak structural features are prone to the initiation of damage cracks, propagation at boundaries under external loads, and interconnection between joints. They directly influence the mechanical behavior and stability of the engineering rock mass. When subjected to mining disturbances, the behavior of the rock mass in jointed and intact zones displays distinct patterns of damage and instability, collectively impacting the overall mechanical characteristics of the excavation. Therefore, the study of coalescent fracture and instability evolution patterns between jointed and intact regions in jointed rock is of paramount importance.

Relevant scholars have conducted extensive research, exploring the failure and instability characteristics of jointed rock masses at both microscopic and macroscopic scales. These studies have primarily focused on aspects such as rock joint filling materials, dip angles, and connectivity. Regarding research on the mechanical properties and failure characteristics of jointed rocks with filled joints, scholars generally hold the following understandings: The shear strength of filled joints is determined by the combined effects of normal stress, filling thickness, and filling material saturation [1,2]. The degree of joint filling directly affects the mechanical performance and failure modes of rock joints [3]. The failure of jointed rock with filling initially occurs at the contact surface between joints and filling materials, followed by the failure of the filling medium [4]. The energy dissipation of rocks is inversely correlated with the thickness of joint filling and positively correlated with the strength of filling materials [5].

In the research concerning rock joint dip angles and connectivity, it has been observed that the pre-peak energy self-inhibition effect in jointed rock increases with an increasing joint dip angle, initially strengthening and subsequently weakening. This effect exhibits a positive correlation with joint length [6]. The sequence of failure in jointed rock undergoes changes as the joint dip angle increases, transitioning from filled-type weak joints to the rock matrix [7]. Joint dip angles of 45° and 90° exert the most significant influence on the mechanical properties of jointed rock, while the impact is minimal at a 15° dip angle [8]. Non-connected joints noticeably degrade the rock mass, with the strength of jointed rock positively associated with the joint dip angle. With increasing joint connectivity, the fracture toughness of jointed rock follows an approximately hyperbolic trend, decreasing [9]. An equivalent elastic model for rock masses featuring intersecting connected and non-connected joints has been developed using the equivalent elastic modeling approach [10].

In recent years, many coal mines in eastern China have reached depths exceeding one kilometer, resulting in extensive bidirectional jointing within the surrounding rock of tunnels, especially under high stress and intense mining conditions. This has contributed to increased complexity in the discontinuity and deformation damage of the surrounding rock. The process of crack propagation in rock specimens with two joints differs from that in specimens with a single joint, and the development of cracks is influenced by factors such as joint spacing, dip angle, and location. Consequently, numerous scholars have delved into the mechanisms of crack propagation through the interaction of two joints.

In the case of layered jointed rock masses, as the joint angle increases, the impact of joint surfaces on failure characteristics decreases [11]. In non-connected jointed rock masses during unloading, the maximum shear stress occurs on both sides of the joint, followed by the center of the rock bridge, while the joint surface experiences the minimum shear stress [12]. The numerical values of elastic strain energy and dissipation energy for double-jointed rock specimens exhibit significantly smaller abrupt increases or decreases compared to single-jointed specimens [13]. Under dynamic loading, specimens with double cracks at different angles display an X-shaped distribution of the primary fracture [14]. In jointed rock masses, coplanar joint tips predominantly undergo pure shear failure, while adjacent joint tips experience both tension and shear failures. Non-coplanar joints primarily exhibit a combination of shear and tension failures [15]. The deformation and damage process of prefabricated jointed rock masses under freeze–thaw cycles can be divided into four stages: compaction, elastic deformation, pre-peak instability, and post-peak instability damage [16]. Additionally, the mechanical properties of defective red sandstone are weakened due to the pore pressure from free water [17]. During stress, defective rocks primarily exhibit shear cracking, and at low crack inclinations ($\alpha < 45$ degrees), there is a notable formation of concentrated zones [18].

The previously mentioned research has extensively investigated various aspects of jointed rock, encompassing its failure modes, deformation characteristics, and the influence of mechanical parameters. Most scholars have directed their research efforts toward jointed rock masses, with a predominant focus on damage mechanics and fracture mechanics. They have explored the effects of various spatial distributions, such as angles and widths, as well as the filling characteristics of joints on the mechanical properties of rock masses. Additionally, they have delved into patterns of macro and micro-scale crack propagation. Nonetheless, there is a notable scarcity of research on the deformation and evolution processes of jointed rock masses with multiple joints, particularly in terms of analyzing their mutual interactions. A deeper, more comprehensive analysis in this realm is clearly warranted.

This study entails the design of red sandstone specimens with dual joints, positioned at a 45-degree dip angle, varying in length. Cement slurry is used to fill these dual joints, allowing for the differentiation between the jointed and intact regions. Subsequently, laboratory compression tests are conducted to investigate the slip, propagation of secondary cracks, and distribution patterns of deformation fields in the dual-jointed rock during the loading process. Furthermore, numerical simulations of jointed rock are executed to clarify

the fracture and instability characteristics influenced by joint response between jointed and intact regions in 45-degree dual-jointed rock. The study also encompasses the identification of physical data at critical nodes throughout the loading process.

2. Experimental Research

2.1. Preparation of Pre-Fabricated Jointed Red Sandstone

In accordance with international standards for rock mechanics testing, we meticulously processed the red sandstone into standardized rectangular rock specimens measuring 50 mm × 50 mm × 100 mm (length × width × height). To replicate the presence of natural joints in the rock, we utilized a rock-cutting machine to create varying-sized cracks along both sides of the red sandstone samples, subsequently filling these fissures with cement slurry. Within a controlled indoor environment, the cement slurry was meticulously prepared by blending 325-grade cement and water, maintaining a cement-to-water mass ratio of 2:1. The outcomes of rock mechanics testing revealed that the compressive strength of the standard cement sample, featuring a water-to-cement ratio of 0.5, measured 32 MPa, while the tensile strength reached 5.5 MPa, and the density stood at 3.0 g/cm³. The pristine red sandstone specimens demonstrated a uniaxial compressive strength of 50.7 MPa, representing an 18.7 MPa advantage over the standard cement sample (with a water-to-cement ratio of 0.5). Consequently, the dissimilarity in strength could be effectively simulated using cement slurry to replicate structural characteristics.

2.2. Design of Experimental Plan

This experiment was designed with four sets of jointed rock specimens, and the experimental setup is detailed in Table 1 and Figure 1. Initially, a cutting machine was used to create incisions in the red sandstone, ensuring an average width of 5 mm for each cut and an elliptical shape at the ends of the incisions. Subsequently, a cement slurry was injected into these incisions using a syringe, and waterproof tape was used to secure it to the surface of the red sandstone. After the cement slurry filling was completed, the prepared jointed rock specimens (as shown in Figure 2) were placed in an incubator for 28 days. Following the curing period, uniaxial compression tests were conducted on the specimens under servo-controlled displacement loading, with an axial displacement rate of 0.001 mm/s.

Table 1. Size design plan for jointed red sandstone.

Numbering	D/mm	H/mm	$\alpha/^\circ$	h/mm	l/mm	l/D	Remark
1-1	50	100	45	35	35	0.7	
1-2	50	100	45	25	25	0.5	
1-3	50	100	45	15	15	0.3	
1-4	50	100	45	0	0	0	Penetration

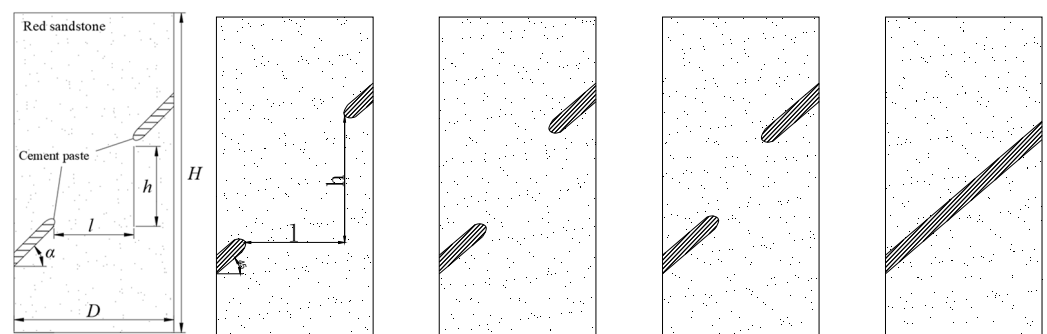


Figure 1. Design scheme for jointed rock mass.

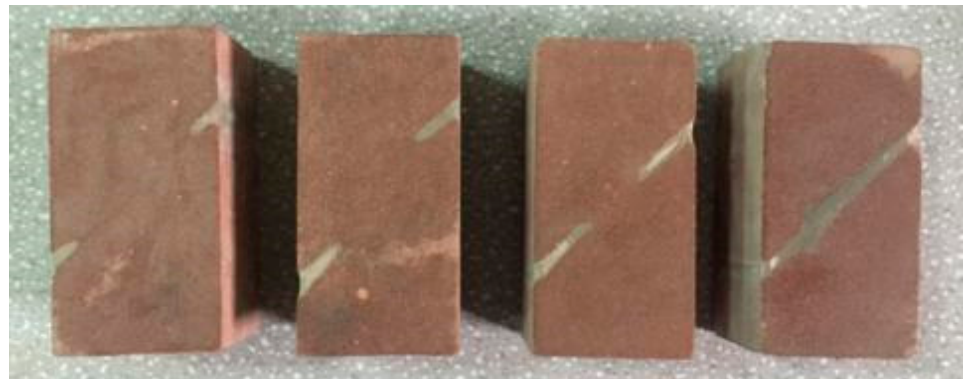


Figure 2. Completed red sandstone jointed rock mass production.

2.3. Test Equipment and System

The experimental testing system comprises the test loading system, acoustic emission device, static strain detection equipment, and image acquisition system. The experiments were conducted using an AG-X250 testing machine (The machine is manufactured by Qingdao Qiankunxing Intelligent Technology Co., Ltd., Qingdao, China) for uniaxial loading, with a loading rate of 0.001 mm/s, and the sensitivity of the testing machine was set to 80%. Simultaneously, a Donghua (Jingjiang, China) DH-3816N static strain testing instrument (as shown in Figure 3a) was used for data acquisition during the experimental process, with a sampling interval of 60 points per minute and a strain sensitivity coefficient ranging from 1.0 to 3.0. BX120-3AA strain gauges (Beijing Yiyang Yingzhen Testing Technology Co., Ltd., Beijing, China) were selected as strain sensors, with a base length \times width of 6.6×3.6 mm and a strain limit of $2000 \mu\text{m}/\text{m}$. Two strain gauges were placed on the surface of each red sandstone specimen, and the sensors were sequentially labeled as S1 and S2 from top to bottom. S1 was oriented perpendicular to the defect trend, while S2 was parallel to the defect trend. The positions of the strain gauges on the intact red sandstone and the four sets of defective rock specimens were identical, as illustrated in Figure 3b, with a physical representation shown in Figure 3c, the device installation location is shown in Figure 4. During the experiment, the MISTRAS series PCI acoustic emission system produced by the American Physical Acoustics Company (Beijing, China) was used to monitor acoustic emission events in the specimens during uniaxial loading. Additionally, a SONY 4K high-speed camera (Sony Corporation, Tokyo, Japan) was employed to capture the entire process of surface crack propagation. Before the experiment, the timing synchronization of the test loading control system, acoustic emission device, and image acquisition equipment was adjusted to ensure their correspondence, The schematic diagram of the testing system is shown in Figure 5.

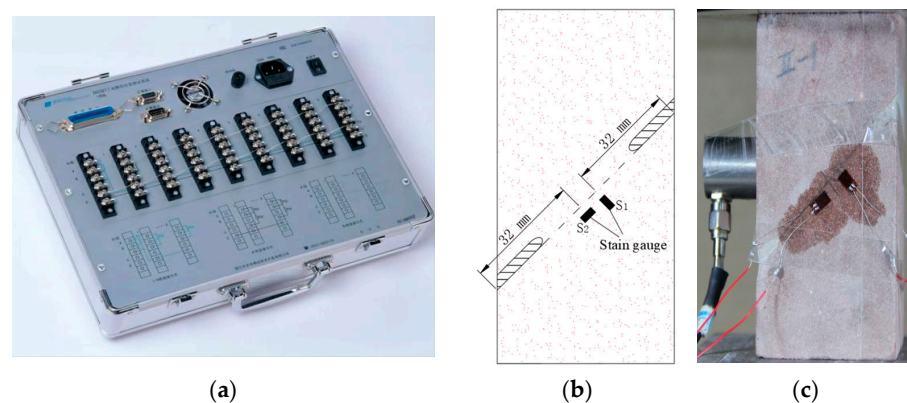


Figure 3. DH-3816N static strain testing system (a); location of strain gauge arrangement (b); physical diagram of sensor layout (c).

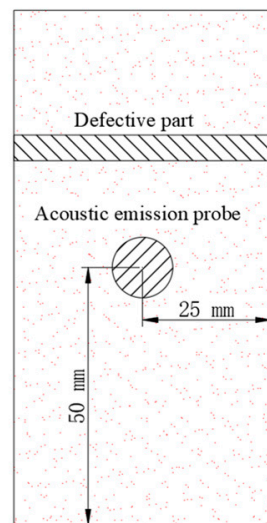


Figure 4. Acoustic emission layout.

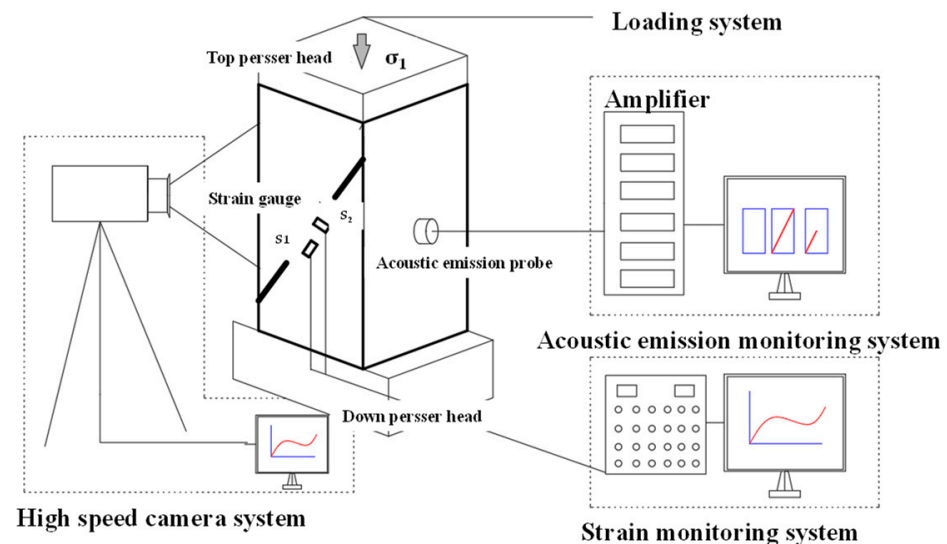


Figure 5. Schematic diagram of the test system.

3. Test Results and Discussion

3.1. Analysis of Strength Variation and Failure Characteristics in Jointed Red Sandstone

The red sandstone specimens used in the experiments include regions with filled joints, and when compared to intact red sandstone, these samples exhibit varying degrees of changes in their mechanical characteristics and deformation properties due to the influence of joints. An analysis of the uniaxial compression test results for these samples reveals noticeable differences in axial stress variations and failure modes among specimens with different joint sizes.

Figure 6 depicts the trends in axial stress over time under uniaxial loading for red sandstone with different joint sizes. The experimental results indicate that, in comparison to red sandstone without joints, the compressive strength of the jointed red sandstone samples No. 1-1 to 1-4 decreased by 9.86%, 45.76%, 40.24%, and 51.68%, respectively. The presence of filled joints results in a reduction in the rock's load-bearing capacity. Additionally, the increase in joint size to some extent contributes to the decreased load-bearing capacity of the rock. Sample No. 1-4 exhibits the most significant decrease in compressive strength.

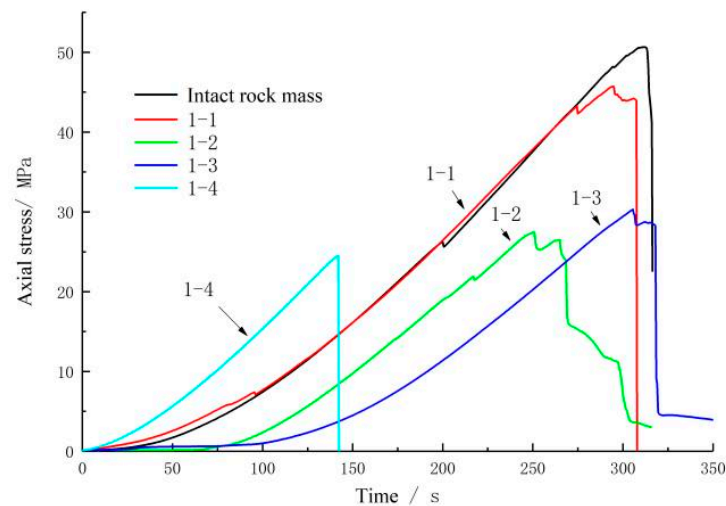


Figure 6. Axial stress vs. time curve of jointed rock mass.

In the jointed red sandstone, tensile failure is the primary mode of failure, accompanied by localized shear failure in the jointed regions, as depicted in Figure 7. Samples No. 1-1 to No. 1-3 all display tension cracks that penetrate the samples at the filled joint ends, propagating perpendicular to the loading direction. In the case of No. 1-4, the filled joint extends across the entire sample, and under the influence of applied stress, the jointed portion of the sample experiences sliding shear failure along the section. The failure modes of the samples indicate that, due to size effects, No. 1-2 initially develops cracks on the specimen's end face during loading, resulting in significant reductions in peak strength due to localized splitting and tensile failure.

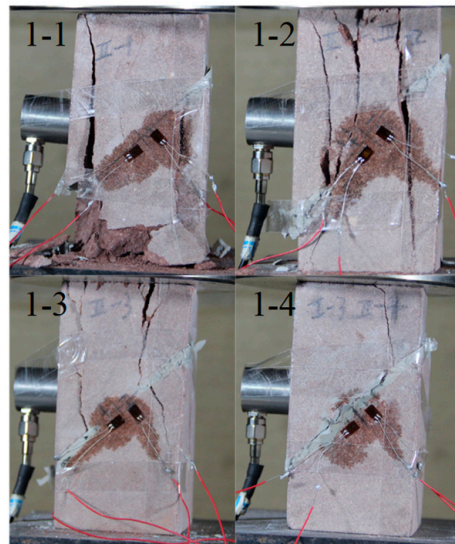


Figure 7. Failure forms of jointed rock masses.

3.2. Analysis of Cooperative Failure Characteristics in Jointed Rock Mass during the Instability Process

3.2.1. Characteristics of Accelerated Interaction Zones during the Instability Process

In conventional uniaxial compression tests, the stress–strain curve for rock can be divided into four segments: the compaction phase (from a to b), elastic phase (from b to c), plastic phase (from c to d), and post-peak phase (from d to e), as illustrated in Figure 8.

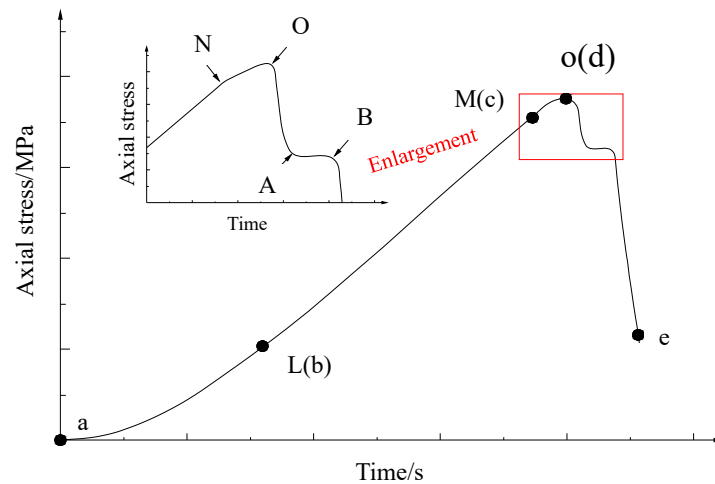


Figure 8. Stress–time curve and instability stage division.

Based on prior research [19,20], it is established that fracture interaction predominantly occurs during the strong non-linear deviation stage and the instability stage. The jointed rock mass exhibits varying physical field information, such as stress and strain, during these different stages. The emergence of cooperation during this phase is attributed to the interaction between strong and weak segments. Typically, before the applied force reaches a certain threshold, the various regional units within the jointed rock mass undergo spontaneous and irregular independent movements with minimal mutual influence. However, as it enters the strong non-linear deviation stage and the instability stage, the correlation between strong and weak segments becomes more pronounced than the independent movement of individual units. This correlation becomes the primary driving force behind cooperative motion among different regions. Consequently, interaction demonstrates zone-specific characteristics.

The study integrates methodologies from prior research to classify the strong non-linear deviation stage, sub-instability stage, and instability stage. Figure 8 illustrates the stress–time curve derived from the stress–strain curve obtained via the loading test machine. Critical stress values at key moments are identified with letters.

The LM (b-c) segment signifies the linear deformation stage, characterized by elastic deformation in the rock, with the elastic model remaining essentially constant during this phase.

The MO (c-d) segment marks the departure from linearity, where the stress–strain curve exhibits an upward concave trend. This phase involves microcracking and plastic deformation in the rock, accompanied by changes in the stress field. The NO subsegment represents a significant departure from linearity, featuring a slower rate of stress increase.

The OB segment represents the sub-instability stage, featuring a post-peak drop in the curve as internal rock fractures expand and connect. Within this stage, the OA subsegment represents a static sub-instability stage, with stress changes transitioning to a plateau, decline, or stable fluctuations in the stress–time curve. The AB subsegment represents a dynamic sub-instability stage, characterized by a rapid decline in the curve.

The sub-instability stage OB lies between the stress peak point and the rapid instability point. During this stage, the stress–strain relationship may exhibit non-linear fluctuations. This phase is pivotal as jointed rock masses approach rapid instability, serving as a period of strain accumulation leading to strain release.

3.2.2. Analysis of Cooperative Failure Characteristics in Jointed Red Sandstone

The stress–time trends during the instability stage and the corresponding sample failure modes are illustrated in Figure 9, with crucial points labeled using letters in the stress–time curves. Samples No. 1-1 to 1-4 feature jointed regions of varying sizes, each displaying distinctive failure modes during the loading process.

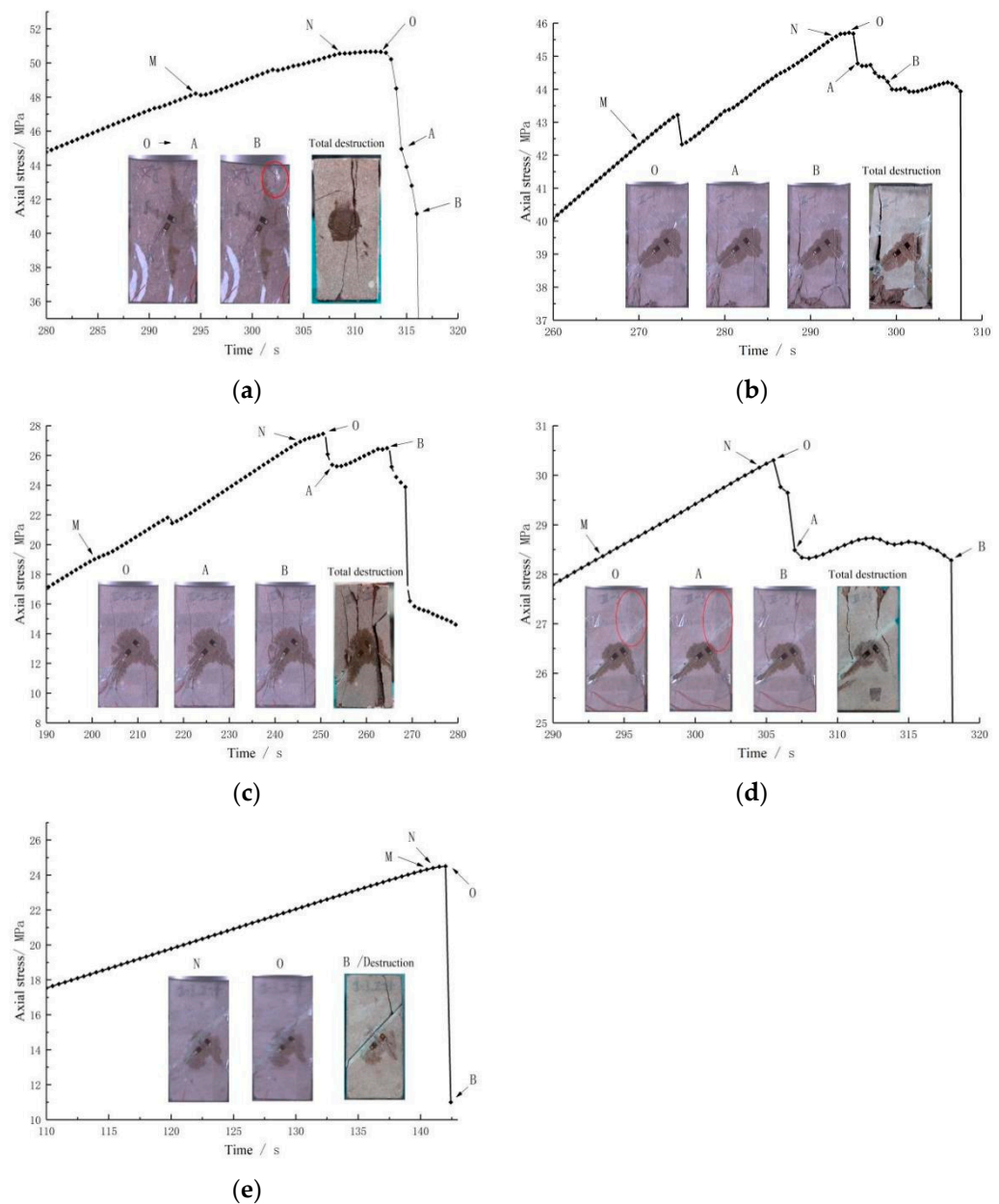


Figure 9. The change of stress at the key points with time and the corresponding failure mode. (a) Complete red sandstone; (b) No. 1-1 ($l/D = 0.7$); (c) No. 1-2 ($l/D = 0.5$); (d) No. 1-3 ($l/D = 0.3$); (e) No. 1-4 ($l/D = 0$).

In the case of $l/D = 0.7$ (No. 1-1, Figure 9b), initial cracks emerge at the tips of the lower jointed section of the sample and steadily propagate along the axial stress direction. During the O-A stage, the stress curve exhibits a linear decline, and axial stress experiences a sudden drop. Nevertheless, no failure occurs in this stage, as no fresh cracks develop on the sample surface, and existing cracks do not propagate further. Beyond point A in the stress curve, axial stress remains stable and fluctuates until point B, when tensile cracks connect. It is clear that after point B, material failure escalates, and tensile failure becomes the primary mode of specimen failure.

For $l/D = 0.5$ (No. 1-2, Figure 9c), following the attainment of peak strength, initial cracks manifest first at the tips of both the upper and lower jointed sections of the sample. These cracks extend along the axial stress direction after point A. In the A-B stage, the sample undergoes crack propagation and increased damage. Beyond point B, the sample

rapidly dissipates a substantial amount of energy and experiences abrupt failure, leading to a sharp reduction in load-bearing capacity.

In the case of $l/D = 0.3$ (No. 1-3, Figure 9d), during the OB stage, the stress trends and failure modes of sample No. 1-3 resemble those of No. 1-2. The primary failure mode for samples No. 1-2 and No. 1-3 is tensile failure, with rock damage initially occurring at the ends of the jointed regions.

For $l/D = 0.3$ (No. 1-4, Figure 9e), where the joint completely traverses the red sandstone, its failure mode differs from the other samples. Shear failure predominates in this case, with the sample undergoing sliding shear failure along the separation planes of the jointed and intact sections. Localized shear failure gradually progresses to shear failure across the entire cross-section. After loading the sample to point O, numerous cracks develop and extend within the jointed portion until point B, at which the entire sample experiences sliding.

3.3. Sub-Instability Stage Zoning Characteristics in Pre-Fabricated Jointed Red Sandstone

Figure 10 depicts the percentage of the OA segment and AB segment within the sub-instability stage. It is noteworthy that as the joint size increases, the proportion of the static sub-instability stage in relation to the entire sub-instability stage gradually diminishes, while the dynamic sub-instability stage gains prominence. When considering the observed failure modes of jointed red sandstone at different times, it becomes apparent that larger joint sizes lead to a prolonged dissipation of accumulated elastic energy within the red sandstone, resulting in an extended period of rock failure.

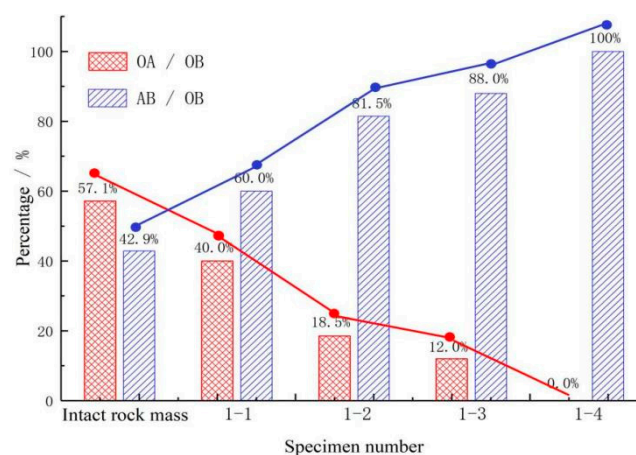


Figure 10. The percentage of OA segment and AB segment in the sub-instability stage.

Upon analyzing data from multiple experimental sets, it becomes evident that jointed rock masses of varying sizes exhibit distinct levels of interaction between the jointed and intact regions during different stress stages in the instability process. The instability process of jointed rock masses can be subdivided into three pivotal stages: the strong departure from the linearity stage (NO), the static sub-stability stage (OA), and the dynamic sub-stability stage (AB). During the strong departure from the linearity stage, the jointed region experiences initial failure, marked by the initiation and propagation of cracks in this area. At this stage, the intact region of the jointed rock mass remains largely undamaged, and the interaction between the jointed and intact regions is relatively weak. The intact region continues to bear the majority of the load. In the sub-instability stage, cracks in the jointed region rapidly extend and interconnect, causing damage to the intact region. During this stage, the interaction between the jointed and intact regions reaches its peak. Upon entering the fully unstable stage, the jointed rock mass experiences complete failure.

3.4. Analysis of Strain Variation in the Intact Region of Rock Mass under the Influence of Joints

(1) Division of Characteristic Strain Change Stages in Jointed Rock Mass. Based on the observed strain change characteristics in Figure 11a,c,e,g, it becomes evident that red sandstone of varying joint sizes exhibits a similar pattern of strain changes in relation to the intact region. These trends can be categorized into three distinct stages:

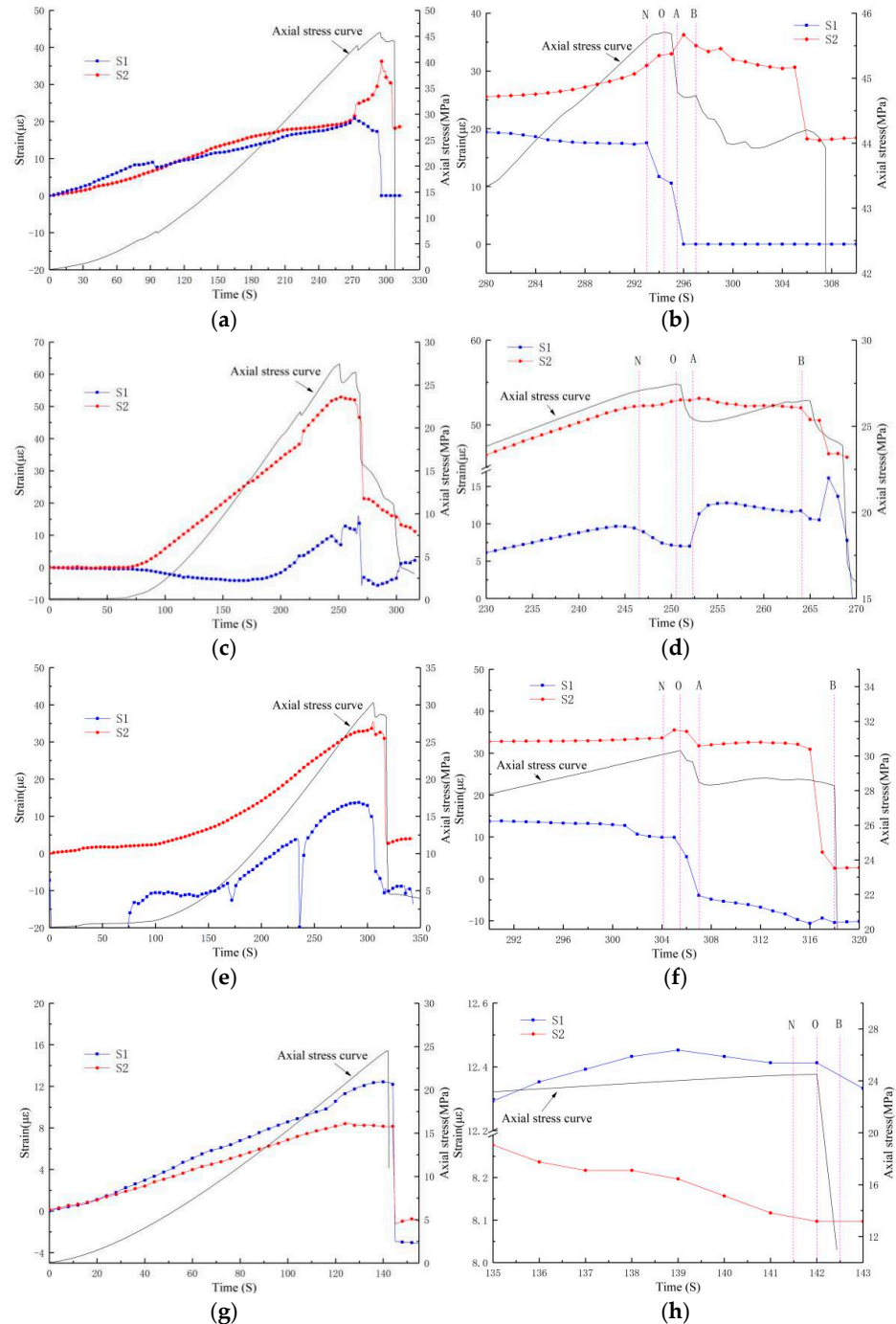


Figure 11. Strain variation characteristics of 11 1-1~1-4 specimens. (a) The strain change of 1-1 specimen in the whole process; (b) the strain change of 1-1 specimen in sub-instability stage; (c) strain changes during the overall process of 1-2 specimens; (d) strain variation during sub instability stage of 1-2 specimens; (e) strain changes during the overall process of 1-3 specimens; (f) strain changes during the sub-instability stage of 1-3 specimens; (g) strain changes during the overall process of 1-4 specimens; (h) the strain change of 1-4 specimen in the sub-instability stage.

① Compaction stage, elastic stage, and early plastic stage: As the applied stress increases, the strain in the jointed region relative to the intact region steadily rises. This is accompanied by localized fluctuations in axial stress.

② Late plastic stage (strong departure from the linearity stage) to sub-instability stage: During this phase, the strain in the jointed region relative to the intact region transitions from gradual fluctuations to abrupt and intense variations. This leads to significant oscillations in strain monitoring data, marking a notable departure from the previous stable changes. Consequently, this stage plays a critical role in identifying when the rock mass enters a state of complete instability.

③ Instability stage: In this stage, the test specimen has undergone complete failure. The strain in the jointed region relative to the intact region stabilizes at a specific value or reverts to zero, indicating the complete failure of the specimen.

(2) Sub-Instability Stage Strain Transient Characteristics in Jointed Rock Mass

Sample 1-4, influenced by shear failure, did not exhibit a typical sub-instability stage, and its strain changes differed significantly from those of the other specimens.

In Sample 1-1, Strain S1 displayed the following pattern: an accelerated increase during the NO stage ($+2 \mu\epsilon$), followed by relative stability during the OA stage, and a sudden sharp increase followed by a sharp decrease during the AB stage ($+5 \mu\epsilon$ to $-4 \mu\epsilon$). On the other hand, Strain S2 showed a sharp decrease during the NO stage ($-7 \mu\epsilon$), followed by relative stability during the OA stage, and a rapid decrease to zero during the AB stage ($-10 \mu\epsilon$), as depicted in Figure 11b. Consequently, during the strong departure from the linearity stage (NO), the jointed rock mass initially emits instability signals, such as a sudden increase or decrease in strain, although the magnitude of these signals is relatively low. In the static sub-instability stage (OA), the jointed rock mass maintains a phase of stability. In the dynamic sub-instability stage (AB), the jointed rock mass releases intense instability signals, with strain changes reaching as high as 50%. This stage serves as a precursor to the complete instability of the jointed rock mass.

In Samples 1-2 and 1-3, Strains S1 and S2 exhibited a similar trend to that of Sample 1-1 during the N-B stage, characterized by significant strain changes in the NO stage and rapid changes in the AB stage. However, the extent of strain variation in Samples 1-2 and 1-3 was lower compared to Sample 1-1. This phenomenon can be attributed to differences in the sizes of the jointed portions. In fixed-sized red sandstone samples, as the proportion of the jointed portion increases, its influence on the intact portion of the red sandstone becomes more pronounced. Under the same external loading conditions, when the proportion of the jointed portion is relatively small (as in Sample 1-1), the strain energy released due to the jointed portion's failure is lower, resulting in a relatively higher accumulation of strain energy in the intact portion of the red sandstone. Consequently, the physical signals released during the instability process (with strain gauges located in the intact portion) become more pronounced. Conversely, when the joint proportion is larger (as shown in Figure 11b), the jointed portion concentrates stress to a greater extent, causing a higher release of strain energy. The specific areas of mutual influence are shown in Figure 12. Consequently, the physical signals released during the instability process in the intact portion become less prominent.

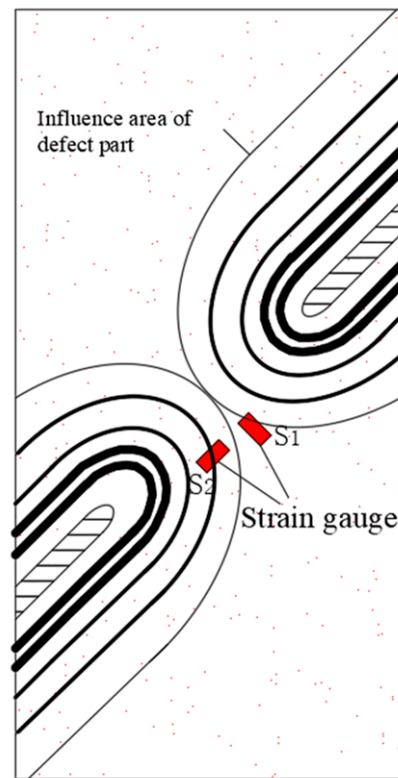


Figure 12. Synergistic influence area.

3.5. Analysis of Acoustic Emission Characteristics during the Instability Process of Jointed Red Sandstone

Figure 13 illustrates the acoustic emission signal characteristics during the sub-instability stage for the four test specimens. From the acoustic emission monitoring data, it is evident that Sample 1-4, which experienced sudden shear instability, did not generate a significant number of AE events during the instability stage. However, at 137 s in Sample 1-4, the sensor detected an amplitude of 97 dB and an energy of 29,000, which corresponds to the moment when an internal shear crack parallel to the joint orientation occurred within the jointed portion, as observed at the test site.

From Figure 13a–f, it can be observed that Samples 1-1, 1-2, and 1-3 did not produce significant acoustic emission signals during the strong departure from the linearity stage (NO). However, during the strong departure from the linearity stage (NO), they began to generate noticeable acoustic emission events, with amplitudes around 85 dB and energy levels below 5000.

During the static sub-instability stage (OA), these specimens consistently produced intense acoustic emission signals. Notably, Sample 1-2 exhibited a peak in acoustic emission signals with an amplitude of up to 97 dB and energy levels as high as 16,000.

In the dynamic sub-instability stage (AB), as the specimens gradually lost stability and cracks initiated and propagated, they produced a continuous stream of acoustic emission signals. Analyzing the acoustic emission characteristics of the jointed rock mass reveals that as it enters the strong departure from the linearity stage and sub-instability stage, it consistently generates acoustic emission signals. The amplitudes and energy levels of these signals initially peak during the loading process. The continuous generation of these acoustic emission signals signifies that the jointed rock mass is approaching failure. Therefore, it can be inferred that the onset of the sub-instability stage marks the beginning of cooperative failure in the jointed rock mass.

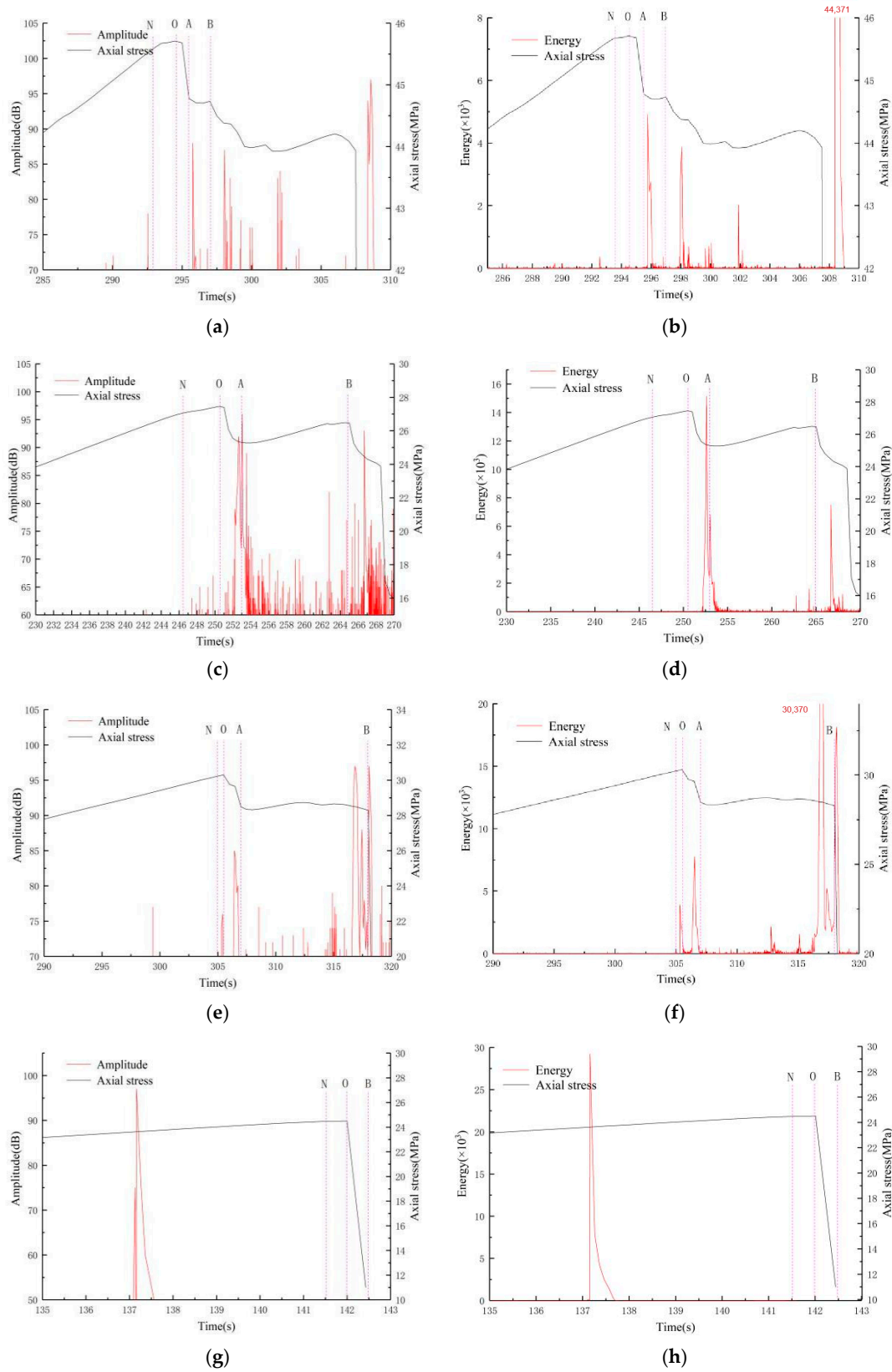


Figure 13. Analysis of acoustic emission results of 1-1~1-4 specimens. (a) Time–amplitude–stress of 1-1 specimen; (b) time–energy–stress of 1-1 specimen; (c) time–amplitude–stress of 1-2 specimen; (d) time–energy–stress of 1-2 specimen; (e) time–amplitude–stress of 1-3 specimen; (f) time–energy–stress of 1-3 specimen; (g) time–amplitude–stress of 1-4 specimen; (h) time–energy–stress of 1-4 specimen.

4. Detailed Mechanical Response of Jointed Red Sandstone Model Specimens

In the preceding sections, we explored the crack propagation and failure patterns of a set of prefabricated jointed rock specimens through uniaxial compression tests. The mechanical behavior under uniaxial compression primarily involves a mixed tensile–shear failure, so using the PFC2D 5.0 numerical simulation software, a two-dimensional fracture mechanics model is established employing the distinct element method (DEM). This modeling encompasses tensile failure induced by tensile strain, and subsequently, the evolution of cracks under uniaxial stress conditions.

4.1. Validation and Application of Fractals

To demonstrate the crack propagation mechanisms discussed in PFC2D, Sample No. 1-3 was modeled as an example. In this case, crack initiation and propagation were tested through uniaxial compression experiments. The geometric structure of the rock model matched that of Sample No. 1-3 in the laboratory experiments, with vertical and horizontal stresses of approximately 20 MPa and 0 MPa, respectively. Based on experimental results with intact red sandstone, the rock had a strength of UCS = 50.7 MPa; cohesion $c = 3.6$ MPa, internal friction angle, tensile strength = 4.0 MPa; Young's modulus $E = 3.0$ GPa; and Poisson's ratio $\nu = 0.24$. Under basic conditions, initial and residual crack apertures were assumed to be 10, with crack shear and normal stiffness at 100 GPa/m. The simulated rock crack propagation of Sample No. 1-3 under uniaxial compression is depicted in Figure 14. During the simulation loading process, small cracks were initially observed at the tip of the end face and propagated in the vertical direction. In the later stages of the simulation, multiple sets of cracks appeared in the rock bridge, and the merging and penetration of these cracks resulted in the failure of rock bridge strength. Based on the numerical simulation results, it can be concluded that crack initiation and propagation are similar to the laboratory test results.

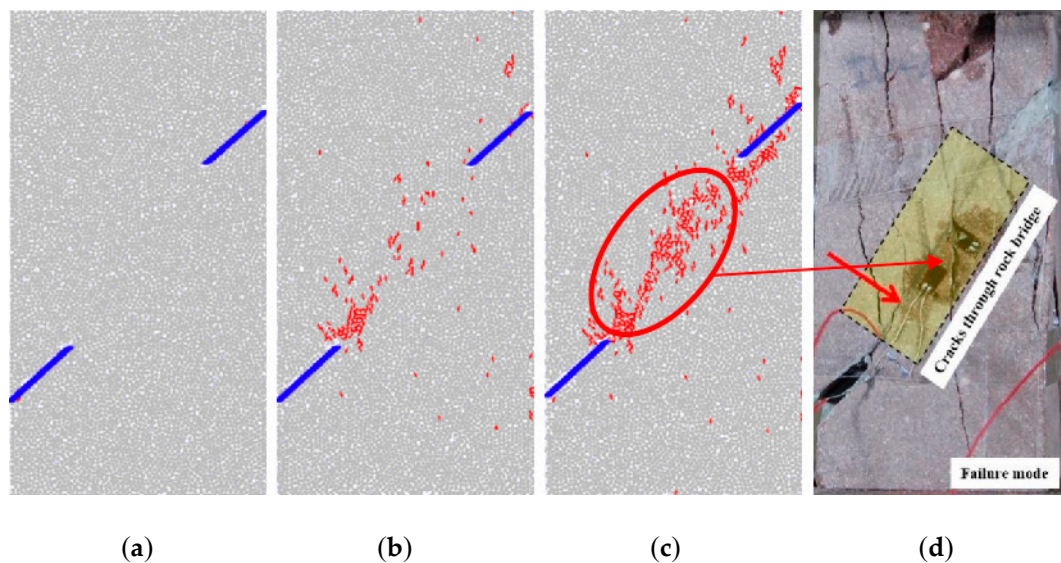


Figure 14. Validation model of rock crack propagation under uniaxial compression. (a) Initial stage of simulation; (b) mid-simulation; (c) the end of simulation; (d) laboratory test.

As shown in Figure 15, based on the computed results, the peak strength data closely match the laboratory results, and the stress–strain curve trends are similar to each other (Figure 15a). In this section, the failure mode of the jointed rock mass is analyzed using the safety factor (Fos). From Figure 15b, we can clearly see that the numerical model effectively simulates the instability and failure process of the rock structure. Under the influence of shear stress, damage to the structure primarily concentrates around the line connecting the two pre-existing fractures, propagating from the crack tips towards the center of the model.

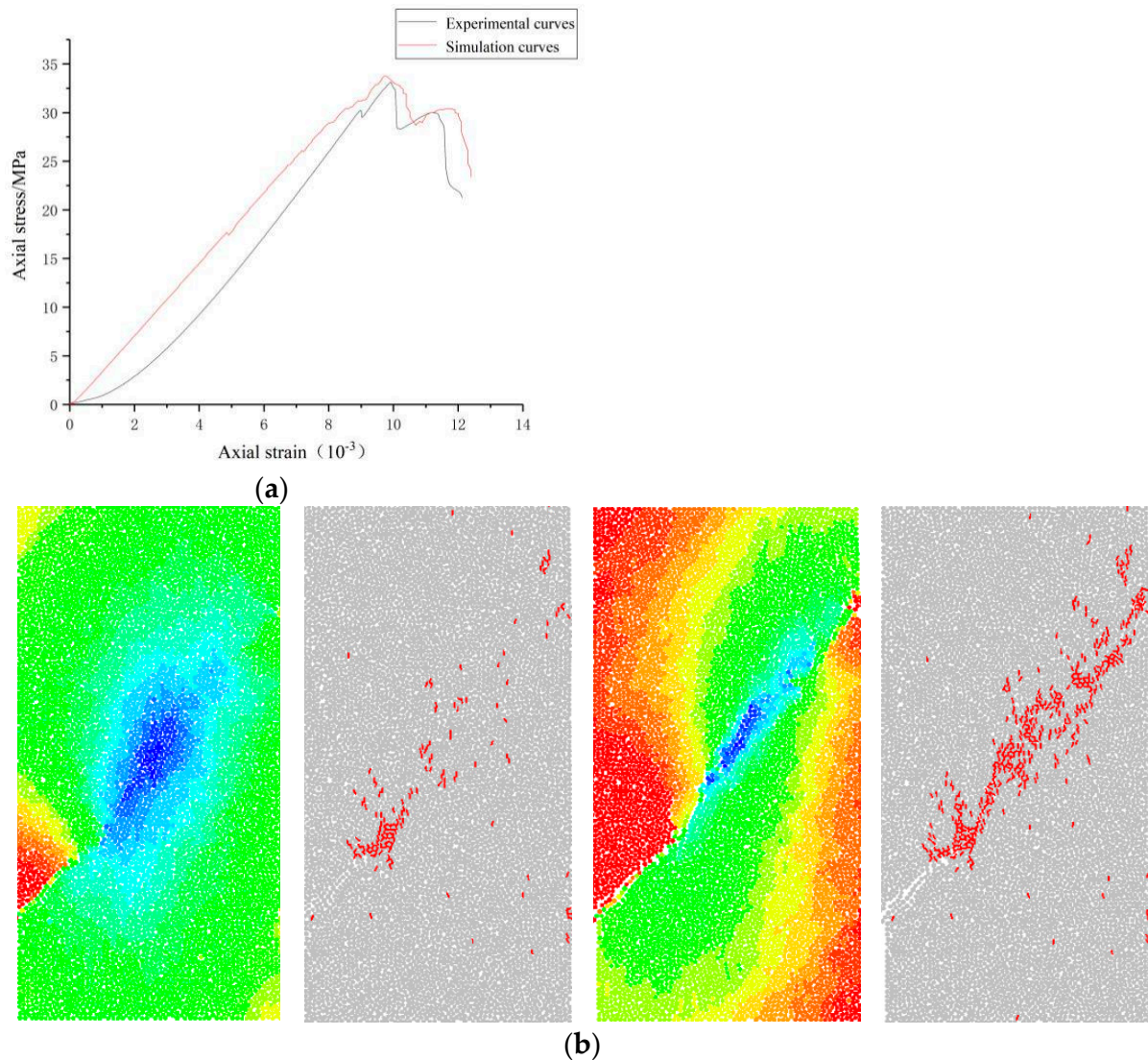


Figure 15. Verification of uniaxial compression test. (a) Axial stress–strain curves in step-by-step calculations and laboratory tests; (b) the results of displacement and crack propagation in numerical simulation.

4.2. Modeling and Simulation Results

In the numerical simulation, the specimen model has dimensions of 50 mm in length and 100 mm in height. The pre-existing fractures in the model are inclined at an angle of 45 degrees, similar to those in Sample No. 1-3. The aperture of these pre-existing fractures measures 5 mm. We have outlined three distinct phases corresponding to different stages, which can be roughly categorized based on the impact of uniaxial loading-induced vertical stress on this jointed rock mass.

Initial loading phase (strong departure from the linearity stage): During this phase, the particle displacement direction at the ends is nearly parallel to the loading direction, influenced by the vertical stresses applied at both ends. The particle displacement direction gradually shifts towards both sides of the model's long axis, with larger angular deviations observed closer to the short axis. At the short axis, particle displacement direction is nearly perpendicular to the model's long axis (Figure 16-NO).

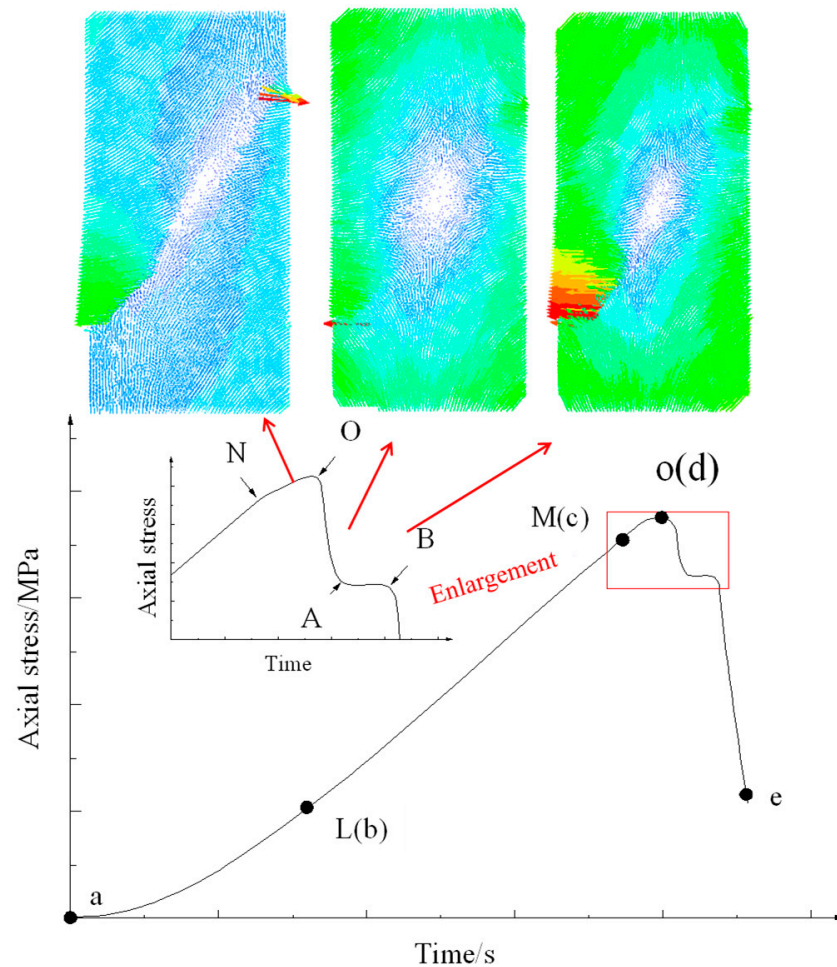


Figure 16. Particle displacement pattern of the model.

Mid-loading phase (sub-instability stage): In this stage, influenced by the pre-existing fractures, there is a sudden change in particle displacement direction near these fractures. At the locations of these fractures, the particle displacement direction is almost perpendicular to the model's long axis. This phenomenon occurs due to the opposite displacement directions on the upper and lower surfaces of the pre-existing fractures, resulting in a 45-degree angle between these surfaces and the loading direction. Consequently, the resultant force is perpendicular to the loading direction. During this phase, differences in particle displacement around the tips of the pre-existing fractures become apparent, with significant variations in particle displacement magnitude and opposing directions on either side of the fracture lines. The model begins to exhibit shear failure tendencies (Figure 16-OA).

Late-loading phase (instability stage): At this stage, particle displacement directions on either side of the connecting lines between the pre-existing fractures are distinctly opposite, resembling a normal fault. Particles on the upper side move downward, while those on the lower side move upward, with particle displacement directions essentially parallel to the direction of the pre-existing fractures. During this phase, the primary mode of failure in the model is shear failure (Figure 16-AB).

Figure 17 depicts the force chains and crack distribution throughout the loading process of the layered rock. Darker colors and wider lines indicate higher stress concentrations. This process can be roughly categorized into three stages:

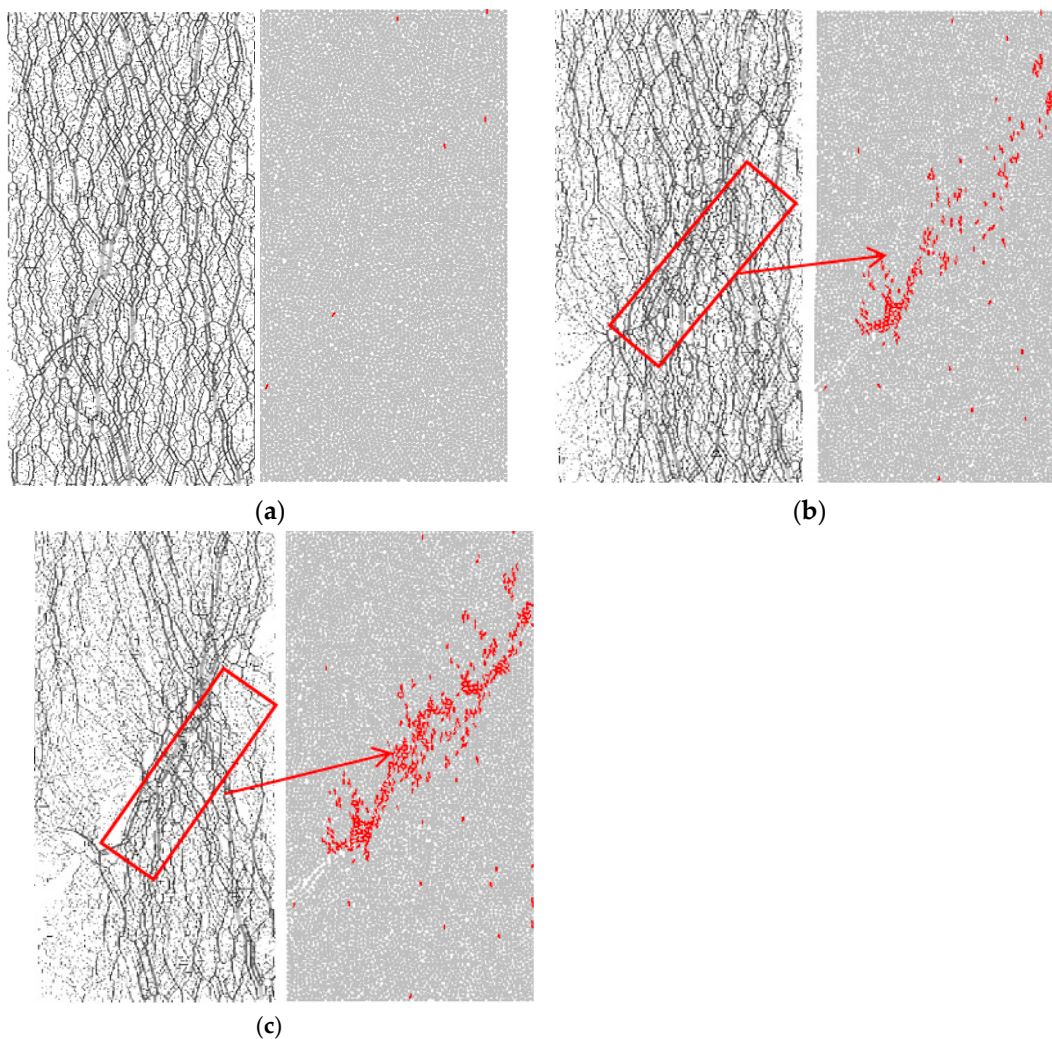


Figure 17. Distribution of force chain and crack in loading process of jointed rock. (a) initial loading; (b) mid loading; (c) end of loading.

Initial loading stage: During this phase, the force chains are distributed relatively evenly within the model.

Mid-loading stage: As pre-existing cracks come into play, stress concentration notably diminishes within the region covered by the horizontal projection of these cracks. Stress is redirected along the model's longitudinal axis towards the interior. Concurrently, stress concentration increases in areas not covered by the horizontal projection of the pre-existing cracks, with the most significant stress concentration occurring around the connecting lines of these two pre-existing cracks.

Late-loading stage: During this phase, the force chains around the connecting lines of the two pre-existing cracks rupture, ultimately leading to the model's destruction. It becomes apparent that there are tensile stresses in the vertical direction and tensile failure cracks surrounding them. Consequently, it can be inferred that the model's failure is predominantly a result of a mixed mode involving both shear and tensile failure.

5. Conclusions

Through indoor rock mechanics experiments, we have explored the interplay between robust and weaker segments within jointed rock masses throughout the failure process. By gathering an extensive array of physical field data, encompassing stress, strain, and acoustic emissions, we have undertaken a comprehensive analysis of the transfor-

mation of jointed rock masses from individual behavior to collective failure just before reaching instability.

(1) Under the influence of stress, the primary load-bearing components within the jointed rock mass are the comparatively sturdy ones. Initially, the less robust segments within the rock mass undergo weakening and evolve into regions of strain release. As these points of strain release and interconnect and the release areas expand, the overall strain accumulation intensifies due to interactions, eventually leading to the rapid failure zones.

(2) During the strongly non-linear phase, jointed rock masses emit initial indicators of instability, such as abrupt increases or decreases in strain (or continuous acoustic emission signals). However, the extent of signals released during this phase is relatively limited. In the sub-instability phase, the rock mass emits pronounced signals of instability, with strain changes reaching levels of up to 50% (with amplitude and energy reaching their first peak). The continuous generation of physical signals during this phase signifies that the jointed rock mass is on the brink of failure. Therefore, it can be inferred that the entry into the sub-instability phase marks the onset of cooperative failure.

(3) The entry into the sub-instability phase symbolizes the initiation of cooperative failure. During the strongly non-linear phase, isolated regions of strain accumulation and release points initially emerge within the weaker segments and influence the interfaces between the jointed and intact regions. In the static sub-instability phase, interactions commence, and the regions of strain accumulation within the jointed areas multiply and rapidly expand, impacting the accumulation of strain in the intact regions. As we progress into the dynamic sub-instability phase, there is mutual connection and interaction between the strain release points in the jointed and intact regions, resulting in an intensified cooperative process that reaches its peak intensity. Subsequently, the rock mass undergoes a transition into complete instability.

Author Contributions: Conceptualization, B.Z. and S.Z.; methodology, B.S.; software, X.H. and B.S.; validation, S.S.; formal analysis, Y.L.; investigation, B.Z.; resources, B.Z.; data curation, X.H. and Y.L.; writing—original draft preparation, B.Z.; writing—review and editing, B.Z.; visualization, S.Z. and S.S.; supervision, B.S.; project administration, S.Z.; funding acquisition, S.Z. All authors have read and agreed to the published version of the manuscript.

Funding: This research was funded by the Open Fund of State Key Laboratory of Water Resource Protection and Utilization in Coal Mining (No. GJNY-20-113-19), National Natural Science Foundation of China (No. 52004147, 51974173).

Institutional Review Board Statement: Not applicable.

Informed Consent Statement: Not applicable.

Data Availability Statement: The original contributions presented in the study are included in the article, further inquiries can be directed to the corresponding author.

Conflicts of Interest: The authors declare no conflicts of interest.

References

- Jiao, F.; Xu, J.; Guo, B.; Peng, S.; Yan, F.; Chen, Y. Shear test on the influence of filling thickness on the shear strength of rock joints. *J. Min. Saf. Eng.* **2022**, *39*, 405–412.
- Indraratna, B.; Premadasa, W.; Brown, E.T.; Gens, A.; Heitor, A. Shear strength of rock joints influenced by compacted infill. *Int. J. Rock Mech. Min.* **2014**, *70*, 296–307. [[CrossRef](#)]
- She, C.X.; Sun, F.T. Study of the Peak Shear Strength of a Cement-Filled Hard Rock Joint. *Rock Mech. Rock Eng.* **2018**, *51*, 713–728. [[CrossRef](#)]
- Xiao, W.; Yu, H.; Zhu, Z.; Li, Y.; Liu, W. Experimental study on the dilatancy characteristics of thin-bedded filling rock joints. *Chin. J. Geotech. Eng.* **2020**, *42*, 1499–1508.
- Chai, S.; Wang, H.; Jing, Y.; Jia, N. Experimental study on dynamic compression characteristics of cumulative damage of filled jointed rock. *Chin. J. Rock Mech. Eng.* **2020**, *39*, 2025–2037.
- Wang, G.; Cao, T.; Wen, X.; Sun, F.; Zhang, L. Evolution law of pre-peak energy self-inhibition of single-joint sandstone under uniaxial compression. *J. China Coal Soc.* **2021**, *46* (Suppl. S1), 211–221.

7. Ma, Q.; Su, Q.; Ma, D.; Yuan, P. Experimental study on SHPB dynamic mechanical failure characteristics of sandstone in deep roadway with different joint dip angles. *Chin. J. Rock Mech. Eng.* **2020**, *39*, 1104–1116.
8. Jin, A.; Lu, T.; Wang, B.; Chen, S.; Zhang, J. Experimental study on dip angle characteristics of key joints in rock mass based on improved mechanical equivalence. *Chin. J. Rock Mech. Eng.* **2023**, *42*, 76–87.
9. Liu, T.; Yang, R.; Ding, L.; Li, X.; Zeng, L. Study on mechanical properties and meso-cracking mechanism of granite with non-interpenetrated joints. *Chin. J. Rock Mech. Eng.* **2023**, *42*, 1070–1082.
10. Deng, Z.; Wu, J.; Shang, J.; Xie, L. The equivalent elastic model and strength characteristics of rock mass with transfixion-non-transfixion cross joints. *J. China Coal Soc.* **2018**, *43*, 3098–3106.
11. Li, S.; Lin, H.; Lin, Q.; Wang, Y.; Zhao, Y.; Hu, H. Mechanical behavior and failure characteristics of double-layer composite rock-like specimens with coplanar double joints under uniaxial loading. *Trans. Nonferrous Met. Soc. China* **2023**, *33*, 2815–2831. [[CrossRef](#)]
12. Zhao, Y.; Liu, J.; Jin, A.; Sun, H.; Wang, B.; Wei, Y. Study on failure characteristics of non-interpenetrated jointed rock mass under loading and unloading conditions. *J. Cent. South Univ. (Nat. Sci. Ed.)* **2020**, *51*, 1893–1901.
13. Wang, G.; Zhang, L.; Xu, M.; Liang, Z.; Ran, L. Study on energy evolution mechanism of damage and failure of non-interpenetrated jointed rock mass under uniaxial compression. *Chin. J. Geotech. Eng.* **2019**, *41*, 639–647.
14. Wang, Q.; Xia, K.; Wu, B.; Xu, Y.; Liu, F. Experimental study on dynamic failure of prefabricated parallel double jointed rock-like material plate. *J. Tianjin Univ. (Nat. Sci. Eng.)* **2019**, *52*, 1099–1108.
15. Zare, S.; Karimi-Nasab, S.; Jalalifar, H. Analysis and determination of the behavioral mechanism of rock bridges using experimental and numerical modeling of non-persistent rock joints. *Int. J. Rock Mech. Min.* **2021**, *141*, 104714. [[CrossRef](#)]
16. Wang, J.; Li, J.; Zhou, K.; Jiang, C.; Shen, Y.; Jia, H. Fracture mechanical properties of sandstone with pre-fabricated cracks under freeze-thaw cycles. *Theor. Appl. Fract. Mech.* **2024**, *131*, 104444. [[CrossRef](#)]
17. Yin, T.; Yin, J.; Wu, Y.; Yang, Z.; Liu, X.; Zhuang, D. Water saturation effects on the mechanical characteristics and fracture evolution of sandstone containing pre-existing flaws. *Theor. Appl. Fract. Mech.* **2022**, *122*, 103605. [[CrossRef](#)]
18. Yuan, H.; Xiao, T.; She, H.; Huang, M. Crack propagation law of rock with single fissure based on PFC2D. *Front. Earth Sci.* **2023**, *10*, 977054. [[CrossRef](#)]
19. Jin, M.A.; Guo, Y.S. Accelerated synergism prior to fault instability: Evidence from laboratory experiments and an earthquake case. *Seismol. Geol.* **2014**, *36*, 547–561.
20. Jin, M.A.; Sherman, S.I.; Guo, Y.S. Identification of meta-instable stress state based on experimental study of evolution of the temperature field during stick-slip instability on a 5° bending fault. *Sci. China Earth Sci.* **2012**, *55*, 869–881. [[CrossRef](#)]

Disclaimer/Publisher’s Note: The statements, opinions and data contained in all publications are solely those of the individual author(s) and contributor(s) and not of MDPI and/or the editor(s). MDPI and/or the editor(s) disclaim responsibility for any injury to people or property resulting from any ideas, methods, instructions or products referred to in the content.